



**HAL**  
open science

# Numerical modeling of fracture process using a new fracture constitutive model with applications to 2D and 3D engineering cases

Junchao Chen, Lei Zhou, Alexandre Chemenda, Binwei Xia, Xiaopeng Su,  
Zhonghui Shen

## ► To cite this version:

Junchao Chen, Lei Zhou, Alexandre Chemenda, Binwei Xia, Xiaopeng Su, et al.. Numerical modeling of fracture process using a new fracture constitutive model with applications to 2D and 3D engineering cases. *Energy Science & Engineering*, 2020, 8 (7), pp.2628-2647. 10.1002/ese3.690 . hal-03003378

**HAL Id: hal-03003378**

**<https://hal.science/hal-03003378>**

Submitted on 1 Dec 2020

**HAL** is a multi-disciplinary open access archive for the deposit and dissemination of scientific research documents, whether they are published or not. The documents may come from teaching and research institutions in France or abroad, or from public or private research centers.

L'archive ouverte pluridisciplinaire **HAL**, est destinée au dépôt et à la diffusion de documents scientifiques de niveau recherche, publiés ou non, émanant des établissements d'enseignement et de recherche français ou étrangers, des laboratoires publics ou privés.



Distributed under a Creative Commons Attribution - NoDerivatives 4.0 International License



## RESEARCH ARTICLE

# Numerical modeling of fracture process using a new fracture constitutive model with applications to 2D and 3D engineering cases

Junchao Chen<sup>1,2</sup> | Lei Zhou<sup>1</sup> | Alexandre I. Chemenda<sup>2</sup> | Binwei Xia<sup>1</sup> | Xiaopeng Su<sup>1</sup> | Zhonghui Shen<sup>1</sup>

<sup>1</sup>State Key Laboratory for the Coal Mine Disaster Dynamics and Controls, Chongqing University, Chongqing, China

<sup>2</sup>CNRS, OCA, IRD, Géoazur, University of Côte d'Azur, Valbonne, France

## Correspondence

Lei Zhou and Binwei Xia, State Key Laboratory for the Coal Mine Disaster Dynamics and Controls, Chongqing University, Chongqing 400044, China. Emails: zhoulei84@cqu.edu.cn (LZ); xbwei33@cqu.edu.cn (BX)

## Funding information

Chongqing Research Program of Basic Research and Frontier Technology, Grant/Award Number: cstc2017jcyjB0252; National Science Fund for Distinguished Young Scholars of China, Grant/Award Number: 51625401; National Natural Science Foundation of China, Grant/Award Number: 51774056 and 51974042; Chongqing University Postgraduates' Innovation Project, Grant/Award Number: CYB17047

## Abstract

The overwhelming majority of experimental and numerical tests show the dependence of mechanical response on discontinuities (such as joints, faults, and bedding plane). In this study, fracture process is numerically investigated using finite-difference method. A quasi-continuum model (assuming that the real rock mass represents the sum of intact rock and fracture) has been developed to describe the fracture propagation in a fractured rock. First, this model has been validated against the experimental results and was shown to simulate satisfactorily the fracture propagation in the tensile, shear as well as the mixed (tensile and shear) modes. This model then has been used to investigate the fracture processes during the 2D long-wall mining and 3D pillar failure. According to the 2D and 3D simulations, it was found that: (a) this model can provide a new reasonable approach to simulating fracture processes in either 2D or 3D cases; (b) roof failure is mainly caused by shear fractures rather than tensile fractures during the 2D long-wall mining.

## KEYWORDS

constitutive model, long-wall mining, pillar failure, shear fracture, tensile fracture

## 1 | INTRODUCTION

Natural discontinuities (eg, joints, faults, and bedding planes) are generated through long-term geological processes. The mechanical response of rock mass is known to be greatly impacted by these discontinuities. The existence of these discontinuities has been the principal obstacle to estimate precisely the deformability and stability of rock masses in practical engineering design. Thus, better interpretation of

such influence is essential to investigate aiming at achieving realistically mechanical response of geo-materials.

Up to now, it has been reported that the formation of these discontinuities most likely correlate with fracture initiation, propagation, and coalescence. More effort therefore has been made to gain better understanding of the mechanism of fracture propagation based on the theoretical analysis<sup>1-6</sup> and available experimental tests.<sup>7-16</sup> These data show that not only the peak strength (at failure) but the

This is an open access article under the terms of the Creative Commons Attribution License, which permits use, distribution and reproduction in any medium, provided the original work is properly cited.

© 2020 The Authors. *Energy Science & Engineering* published by the Society of Chemical Industry and John Wiley & Sons Ltd.

fracture process (eg, initiation, propagation, coalescence, etc) are also strongly dependent on such discontinuities. This indicates that on one hand, the experimental/numerical tests using widely used intact specimen (without discontinuities) are not sufficient to constrain the real rock properties, on the other hand, the comprehensive model involving detailed information of fracture behaviors, in most cases, is not commonly available.

Considering the information achieved, the mechanism of the fracture process within the fractured rock is yet to be fully understood. As a result, different constitutive models (according to continuum or dis-continuum theory) involving the description of fracture behavior also have been proposed, but they were practically not used due to their complexity and limitations. In continuum methodology,<sup>17-20</sup> it was assumed that fractures should be uniformly distributed in each numerical zone. The impact of fractures on mechanical response was regarded as stress-dependent anisotropy of corresponding constitutive parameters (such as Young's modulus, Poisson's ratio) while plastic strain is employed to quantify the displacement discontinuity. However, since plastic strain is irreversible, this is contradictory with the fact that the contact states of fracture (opening, closure, and slippage) are reversible. To solve this problem, in dis-continuum methodology, fracture constitutive models<sup>21-23</sup> have been used to describe the mechanical response (eg, aperture variation, shear dilation, and slippage) for both contact and noncontact state of the fractures. A common view in these models is that rock failure is mainly attributed to the accumulation of open fractures, which are characterized by a constant normal stiffness. These obtained results show that fracture models have the ability to reproduce the real mechanical behaviors within the discontinuous rock mass. However, as mentioned above, on account that these fracture models usually have many parameters and are complex and complicated, they have been not widely used. A fracture constitutive model with simple function is therefore required to describe the fracture behaviors in a fractured rock.

Numerical methods are particularly useful for incorporating the influence of discontinuities on fracture process. Better understanding has been achieved on fracture initiation, propagation, and coalescence in discontinuous rock mass through numerous modeling simulations.<sup>24-31</sup> However, most of these existing methods have their limitations in representing the true physics of fracture behavior. Finite element method<sup>32,33</sup> is the first numerical method adopted to investigate the fracture behaviors, but re-meshing is required while calculating each step of fracture growth. This is time-consuming and may cause possible errors when interpolating variables from the old to the new mesh. Although some authors<sup>34,35</sup> have proposed the extended finite element method (XFEM) to solve the problem of re-meshing, XFEM is still not able to simulate the complex cases of fracture intersections. Discrete

element methods provide good results in modeling fracture propagation, but cannot reflect the real characteristics in continuum field. On another aspect, most of the numerical investigations were focused on the 2D applications and only a few deal with 3D applications of engineering cases, which are typically more complicated, time-consuming, and costly or are impossible via experimental tests. Obviously, 3D analysis is more realistic and suitable for engineering applications.

In the present study, we investigate the fracture process in a fractured rock. This work has been motivated by many recent studies focusing on the fractured rock (using specimens with discontinuities) properties. An original quasi-continuum model is introduced that meets the requirement of being simple and at the same time capturing the principal features of the fracture behaviors. This model has been implemented into the finite-difference 3-D dynamic time-marching explicit code Flac3D. The proposed model was tested against the results from two types of experiments on rocks. The verifications show that the code could simulate fracture propagation in a tensile, shear, and the mixed (tensile and shear) modes. This model then has been used to investigate the fracture processes in the 2D long-wall mining and 3D pillar failure.

## 2 | GOVERNING EQUATIONS

### 2.1 | Geomechanical model

The linear elasticity theory is adopted to describe the mechanical behavior of rock formations, which includes the equilibrium equation Equation (1), the geometrical equation Equation (2) and constitutive equation Equation (3)

$$\sigma_{ij,j} + \rho \left( b_i - \frac{dv_i}{dt} \right) = 0 \quad (1)$$

$$\epsilon_{ij} = \frac{1}{2} (u_{i,j} + u_{j,i}) \quad (2)$$

$$d\sigma_{ij} = 2Gd\epsilon_{ij} + \alpha_1 d\epsilon_{kk} \delta_{ij} \quad (3)$$

where  $\rho$  is the rock density ( $\text{kg/m}^3$ );  $\mathbf{b}$  is the body force vector per unit volume ( $\text{m/s}^2$ );  $\mathbf{v}$  is the velocity vector ( $\text{m/s}$ );  $E$  is Young's modulus (MPa);  $G$  is shear modulus (MPa);  $\nu$  is Poisson's ratio ( - );  $\alpha_1 = K - 2G/3$ ;  $i, j, k, l \in (1, 2, 3)$ .

According to quasi-continuum theory, fractured rock could be regarded as a mixture of two parts, namely rock matrix element and fracture element (Figure 1). In view of this point, a composed constitutive model is proposed to describe the fracture initiation and propagation in rock matrix elements as well as the fracture behaviors in fractured elements. The theoretical parts of the models are described in detail below.

## 2.2 | Constitutive model for intact rock matrix

In the elastic-plastic domain, the total strain incremental  $d\epsilon_{ij}$  is the sum of elastic  $d\epsilon_{ij}^{el}$  and inelastic  $d\epsilon_{ij}^p$  incremental strains

$$d\epsilon_{ij} = d\epsilon_{ij}^{el} + d\epsilon_{ij}^p \quad (4)$$

where  $d\epsilon_{ij}^{el}$  is defined from Hooke's equations

$$d\epsilon_{ij}^{el} = d\sigma_{kl} / L_{ijkl}^{el} \quad (5)$$

$L_{ijkl}^{el}$  is the elastic stiffness tensor,

$L_{ijkl}^{el} = \alpha_1 \delta_{ij} \delta_{kl} + G (\delta_{ik} \delta_{jl} + \delta_{il} \delta_{kj})$ . The flow rule reads

$$d\epsilon_{ij}^p = d\lambda \frac{dg}{d\sigma_{ij}} \quad (6)$$

where  $d\lambda$  is a non-negative scalar function and  $g$  is the plastic potential function. The yield function used is the classical Mohr-Coulomb criterion (it can be any yield criterion) that is most widely used in rock engineering because of its simplicity. The yield functions (for shear mode in Equation (7) and for tensile mode Equation (8)) read

$$F_s = \sigma_1 - N_\varphi \sigma_3 + 2c \sqrt{N_\varphi} \quad (7)$$

$$F_t = \sigma_3 - \sigma_t \quad (8)$$

where  $N_\varphi = (1 + \sin \varphi) / (1 - \sin \varphi)$ ;  $\varphi$  is the internal friction angle ( $^\circ$ ),  $c$  is the cohesion (MPa). Both  $\varphi$  and  $c$  are defined as usual from the conventional (axisymmetric) compression data that can be presented as  $\sigma_1 (\sigma_3)$  envelope.  $\sigma_t$  is the tensile strength that can be evaluated from direct or indirect tensile tests (MPa). We assume that  $g$  is equal to  $F_s$  and  $F_t$  (associated rule), respectively, for shear and tensile modes. In this study, we use the second strain tensor deviator to evaluate the shear plastic strain.<sup>36</sup> It reads

$$\epsilon_s = \sqrt{\frac{(\epsilon_1^p - \epsilon_2^p)^2 + (\epsilon_2^p - \epsilon_3^p)^2 + (\epsilon_3^p - \epsilon_1^p)^2}{6}} \quad (9)$$

Accordingly, for tensile plastic strain, the maximum tensile strain is employed. It reads

$$\epsilon_t = \epsilon_3^p \quad (10)$$

When the maximum shear (or tensile) strain is reached, calculation element fails. In general, the orientation of fracture is related to rock failure mode. For example, fracture

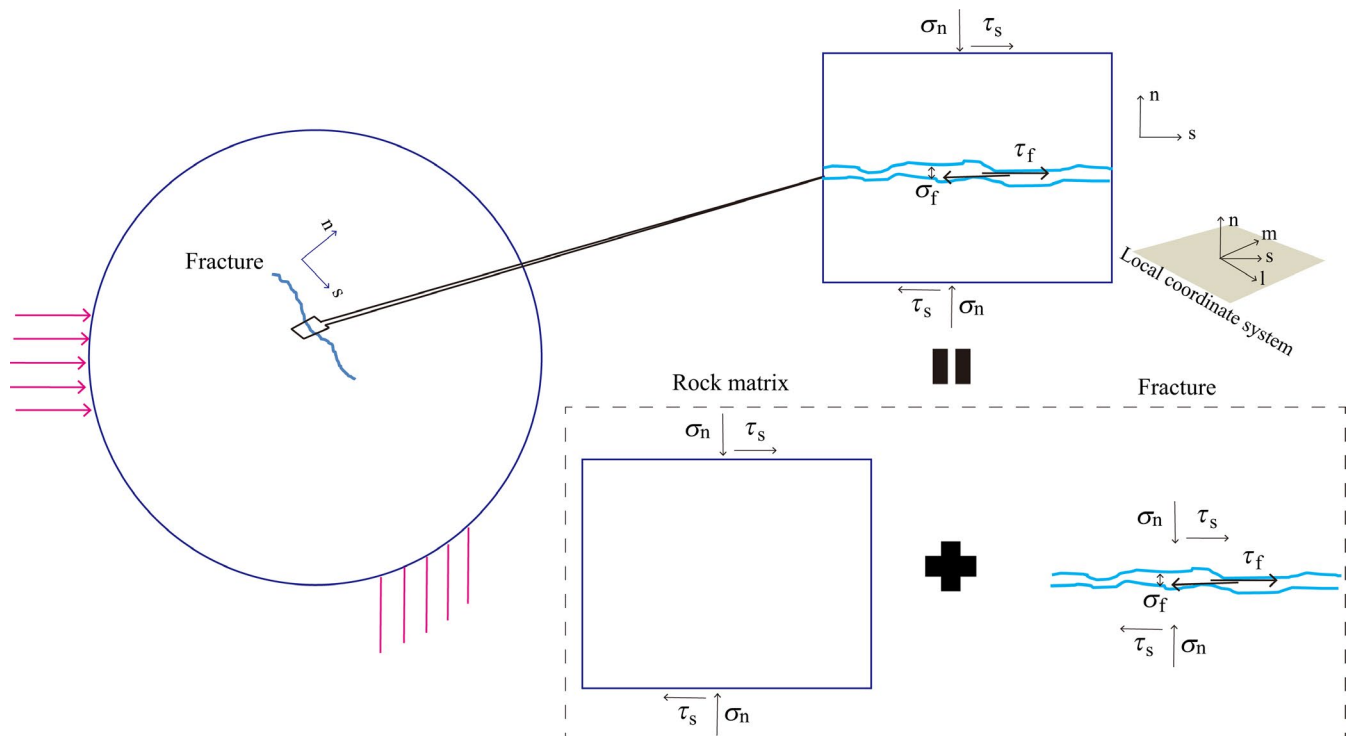
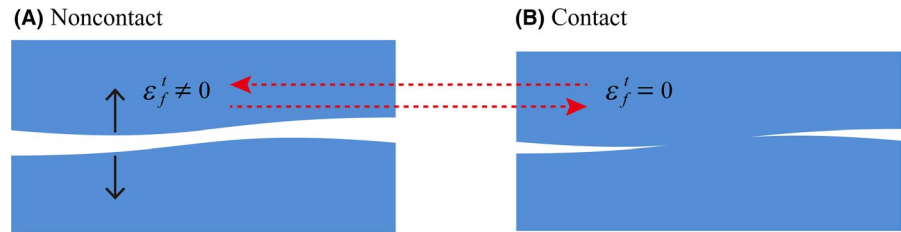


**FIGURE 1** Sketch of quasi-continuum method ( $\sigma_n$  is normal stress;  $\tau_s$  is shear stress;  $\sigma_f$  is normal stress for the fracture;  $\tau_f$  is shear stress for the fracture;  $m, l$  axis in the local coordinate system is decomposed from  $\tau_s$ )

**FIGURE 2** Contact condition of fracture surfaces: (A) noncontact; (B) contact ( $\sigma_f^t$  is tensile stress of the fracture;  $\varepsilon_f^t$  is tensile strain of the fracture)



caused by tensile mode is perpendicular to the maximum tensile principal strain; as for shear fracture, it is generated at the position where it has the least shear strength.

### 2.3 | Constitutive model for the fractured element

According to quasi-continuum theory, the total incremental strain of a fractured element is decomposed on the increment of the elastic strain  $d\varepsilon_{ij}^{el}$  and the fracture elastic strain  $d\varepsilon_{ij}^f$ .<sup>37,38</sup>

Its expression is as follows:

$$d\varepsilon_{ij} = d\varepsilon_{ij}^{el} + d\varepsilon_{ij}^f \quad (11)$$

For the intact part of the fractured element,  $d\varepsilon_{ij}^{el}$  is related

to stresses by Hooke's equations (Equation 5). As for fracture, it includes two cases: contact and noncontact states (Figure 2). For example, for the contact state, the fracture can yield compression and shear stresses; otherwise, the fracture cannot bear any stress for the noncontact condition. Thus, the additional strain caused by the fractures should be respectively calculated with different constitutive models for the two conditions. The brief descriptions are as follows.

#### 2.3.1 | Contact state

For contact state, the normal  $d\varepsilon_{n,1}^f$  and shear  $d\varepsilon_{s,1}^f$  elastic strains are calculated according to Goodman<sup>39</sup> as

$$d\varepsilon_{n,1}^f = d\sigma_n / k_n l_c \quad (12)$$

$$d\varepsilon_{s,1}^f = d\tau_s / k_s l_c \quad (13)$$

where  $\sigma_n$ ,  $\tau_s$  are normal and shear stresses (MPa);  $k_n$ ,  $k_s$  are normal and shear stiffness ( $k_n = k_s = 10$  GPa/m in this study);  $l_c = V/S_c$ , which is the characteristic length of the fracture (m),  $V$  is the volume of the fractured element ( $m^3$ );  $S_c$  is the fracture area in the fractured element ( $m^2$ ). In the contact state, the normal stress imposed to the fracture surface plane is compressive,

which means a nonzero shear stress along the fracture defined as

$$\tau_{\max} = \sigma_n \tan \varphi_f \quad (14)$$

where  $\tan \varphi_f$  is the friction coefficient of the fracture surface and reflects the degree of fracture roughness. Once shear stress exceeds the maximum shear stress, shear slip (or dilation) occurs.

#### 2.3.2 | Noncontact state

In the noncontact state, normal and shear stresses are both zero. In fact, fracture strain is equal to the strain of intact rock matrix. It is calculated as

$$d\varepsilon_{n,2}^f = -\sigma_n / e_1 \quad (15)$$

$$d\varepsilon_{s,2}^f = -\tau_s / 2G \quad (16)$$

where  $e_1 = K + 4G/3$ .

#### 2.3.3 | Transition of the contact state

In reality, the contact state of the fracture surfaces does not remain constant but always changes. The transition of fracture state can be divided into two modes (Figure 2): contact  $\rightarrow$  noncontact; noncontact  $\rightarrow$  contact. Since the normal stress and strain of contact fracture satisfy the elastic relationship in the contact state, in this study, we take strain as criterion. That is, when the tensile strain is generated on the fracture surface, the fracture varies from contact state to noncontact state. On the contrary, when the tensile strain becomes zero, the fracture changes from noncontact state to contact state.

### 2.4 | Solution strategy

The formulated constitutive models have then been implemented into the finite-difference 3-D dynamic time-marching explicit code Flac3D<sup>36</sup> for the numerical modelings in this

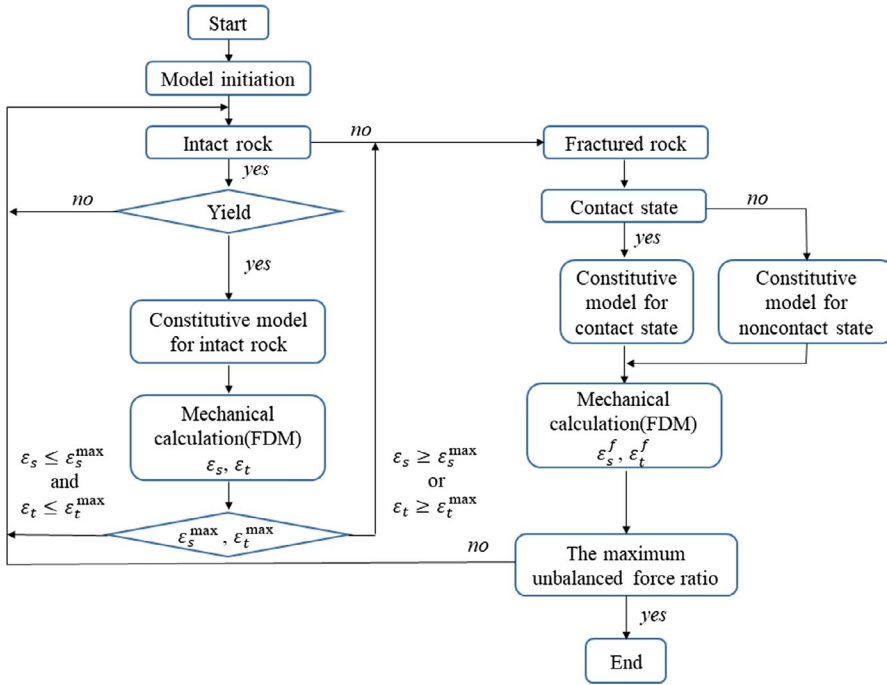


FIGURE 3 Flow chart of the solving procedure

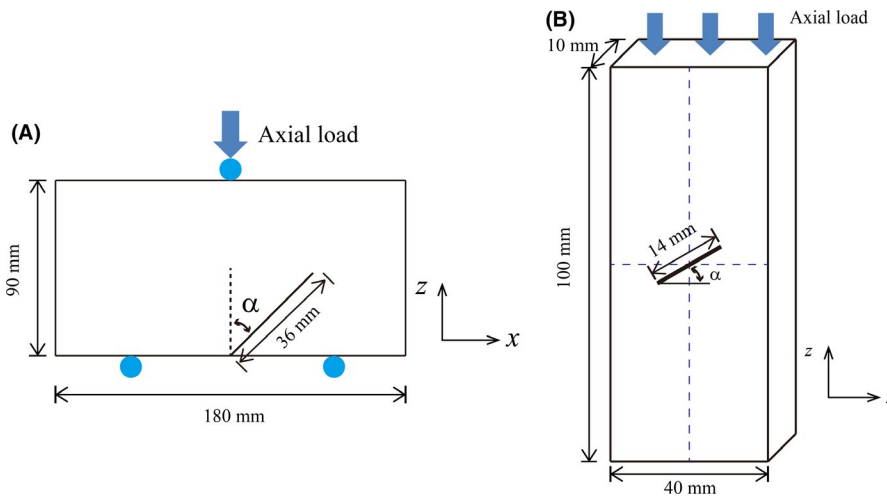


FIGURE 4 Sketch map of rock mechanics tests: (A) three-point bending test; (B) uniaxial compression test

work. The global methodology and procedure for the finite-difference method (FDM) computation is briefly introduced. Figure 3 shows the flow chart of the solving procedure. The solution starts with model initiation. Then, according to the type of calculation elements, different constitutive models are employed for intact (Section 2.2) and fractured (Section 2.3) elements, respectively. For intact elements, the basic variables of elements, such as stress and displacement are computed to obtain the shear and tensile plastic strains. When the obtained either shear or tensile plastic strain in some element exceeds the corresponding maximum value, this element fails and it is immediately changed to fractured element. As for fractured elements, the contact state of the fractures must be first determined based on the description in Section 2.3.3 and then the corresponding constitutive model in Section 2.3 is adopted for continuing computation. The mechanical

calculation terminates once the maximum unbalance force meets the preset error tolerance. To verify the effectivity and applicability of the models, some simulations of traditional rock mechanics tests first are carried out, as described in the next section.

### 3 | VERIFICATIONS

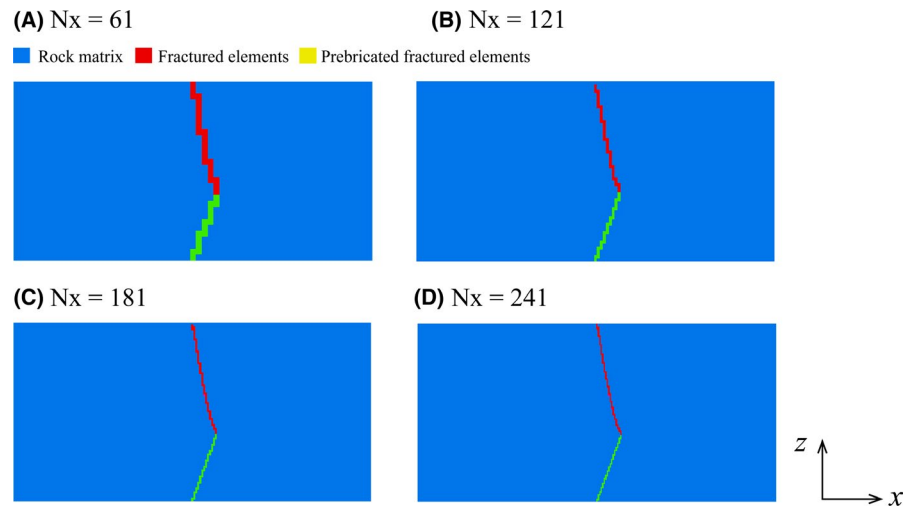
#### 3.1 | Three-point bending tests (specimen with one single flaw)

##### 3.1.1 | Modeling setup

In this case, notched three-point bending tests reported by Luo et al<sup>40</sup> are employed to verify the applicability of the

**TABLE 1** Parameters for sandstone in three-point bending tests

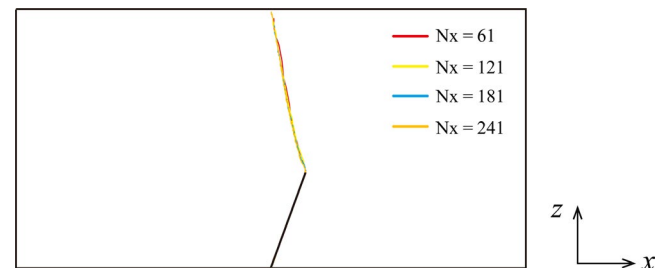
Properties	$E$ , GPa	$\nu$	$c$ , MPa	$\alpha$ , °	$Ten$ , MPa	$\epsilon_{s,max}$	$\epsilon_{t,max}$
Specimen	3.9	0.26	4	35	3.37	0.01	$2.5e-3$
Platen	200	0.1	-	-	-	-	-

**FIGURE 5** Fracture propagations for different grid sizes at  $\alpha = 20^\circ$ .  $N_x$  represents the number of zones in  $x$  direction

proposed model for tensile mode. The modeling setup was designed to be as close to the real experimental conditions as possible. The numerical model consists of three stiff platen (cylinders) and specimen. The sandstone specimens simulated have the same size as the experimental samples,  $180\text{ mm} \times 76\text{ mm} \times 90\text{ mm}$  and contain one central prefabricated flaw (Figure 4A) introduced as a fracture. During the testing process, the downward velocity ( $V_z = -1 \times 10^{-6}\text{ m/s}$ ) is imposed to the upper platen until the model fails. The parameters used for this series are listed in Table 1. Note that since the maximum shear and tensile plastic strain decide how easy the calculation elements are fractured, the fracture process is greatly affected by these values. For all the simulation examples in this study, they are manually adjusted to matching the corresponding experimental tests.

### 3.1.2 | Results

We first begin with testing the role of the grid size (resolution) on the fracture propagation. We use homogeneous brick grids and specimen model sizes  $61 \times 122$ ,  $121 \times 242$ ,  $181 \times 362$  and  $241 \times 482$  numerical zones in the  $x$  and  $z$  directions, respectively.  $N_x$  stands for the number of zones in  $x$  direction. Figure 5 presents fracture propagations for different grid sizes at  $\alpha = 20^\circ$ . It is seen that the isolated failure plane thickness decreases as grid resolution increases. To clearly observe the errors, fracture paths for different grid sizes are illustrated in Figure 6. It shows that fracture path depends on the grid size but very little. Since the objective of this work was to simulate the fracture process,

**FIGURE 6** Fracture path comparison for different grid sizes at  $\alpha = 20^\circ$ 

the following numerical models were performed with  $N_x = 61$  in order to save calculating time.

The curves of load force vs displacement obtained from simulations are illustrated in Figure 7A. It is clear that load force decreases steeply (to approximately zero) until the peak value is reached, which also holds rather common for experimental tests. In addition, good fittings between experimental and numerical results (Figure 7B) are found in the failure strength (peak point at each curve in Figure 7A) as well as its variations with the increase in dip angle.

Figure 8 shows the numerical results of horizontal ( $x$ ) and vertical ( $z$ ) displacement distributions at different dip angles ( $\alpha = 0^\circ, 10^\circ, 20^\circ, 30^\circ, \text{ and } 45.9^\circ$ ). It is clearly observed that the evolution of displacement accompanied with fracture propagation, which allows for the fracture propagation path to be visualized. An example of the horizontal displacement distributions for different calculation steps (Figure 9) and its final grid deformation (added by 10 times horizontal and vertical displacement) at  $\alpha = 20^\circ$  (Figure 10)

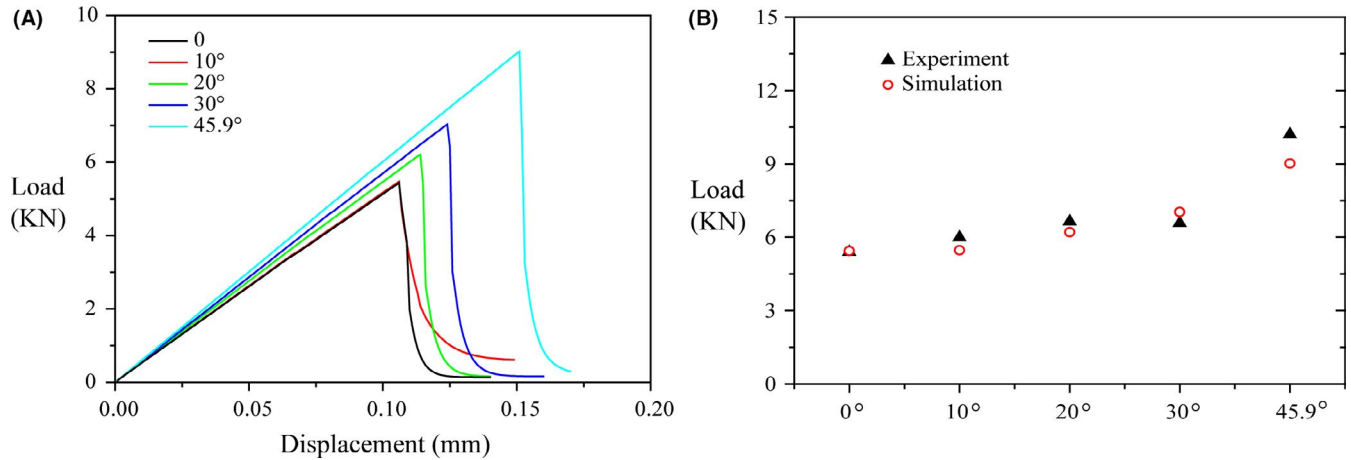


**FIGURE 7** The results of three-point bending tests at different dip angles: (A) stress-strain curves; (B) comparison of peak stresses between numerical and experimental tests

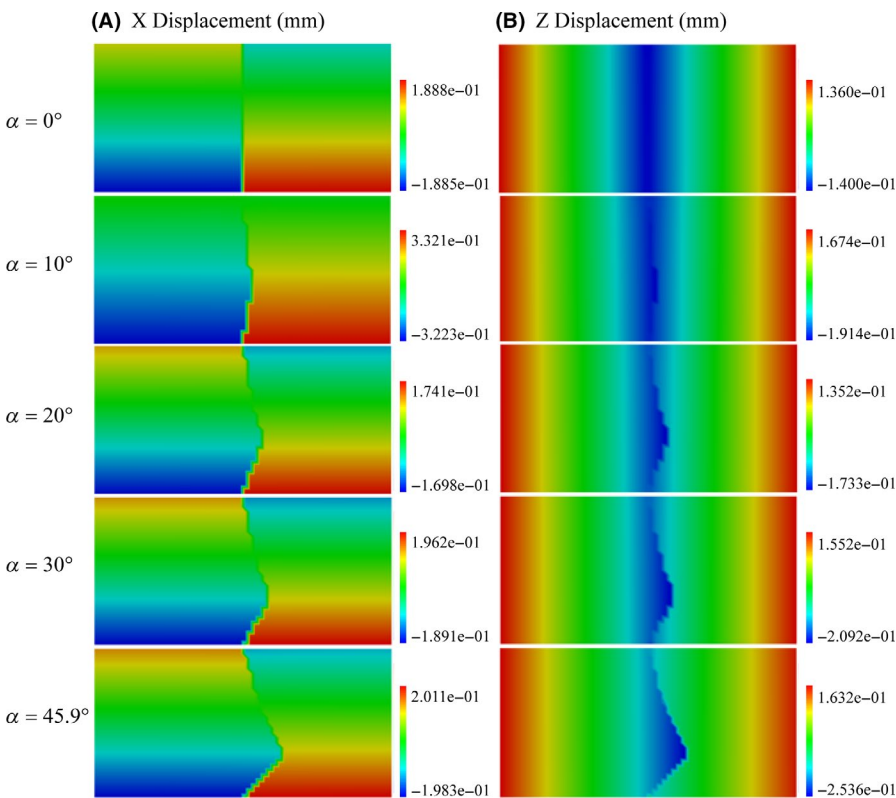


**FIGURE 8** The horizontal (A) and vertical (B) displacement distribution at different dip angles

are presented. It can be seen that first the fracture initiates from the fracture tip and then propagate approximately linearly with terminating at the center of the upper boundary. For convenience in comparison, the outlines of fractures at each dip angle for experiments and simulations are shown in Figure 11. Overall, there are no significant differences in fracture paths between the experimental and numerical results except of the case at  $\alpha = 45.9^\circ$ . The relatively larger discrepancy at  $\alpha = 45.9^\circ$  might be due to the heterogeneity of the experimental specimen. These results suggest the proposed model could simulate the fracture process in the tensile mode.

## 3.2 | Uniaxial compression tests (specimen with one single flaw)

### 3.2.1 | Modeling setup

The experimental tests reported by Zhao et al<sup>14</sup> are taken as an example to confirm fracture initiation and propagation in the shear mode. In this series of tests, the rectangular prismatic rock-like samples ( $40\text{ mm} \times 10\text{ mm} \times 100\text{ mm}$ ) with one central prefabricated flaw (14 mm in length) were used, as shown in Figure 4B. The model includes cuboid specimen and two stiff elastic platens corresponding to steel. The

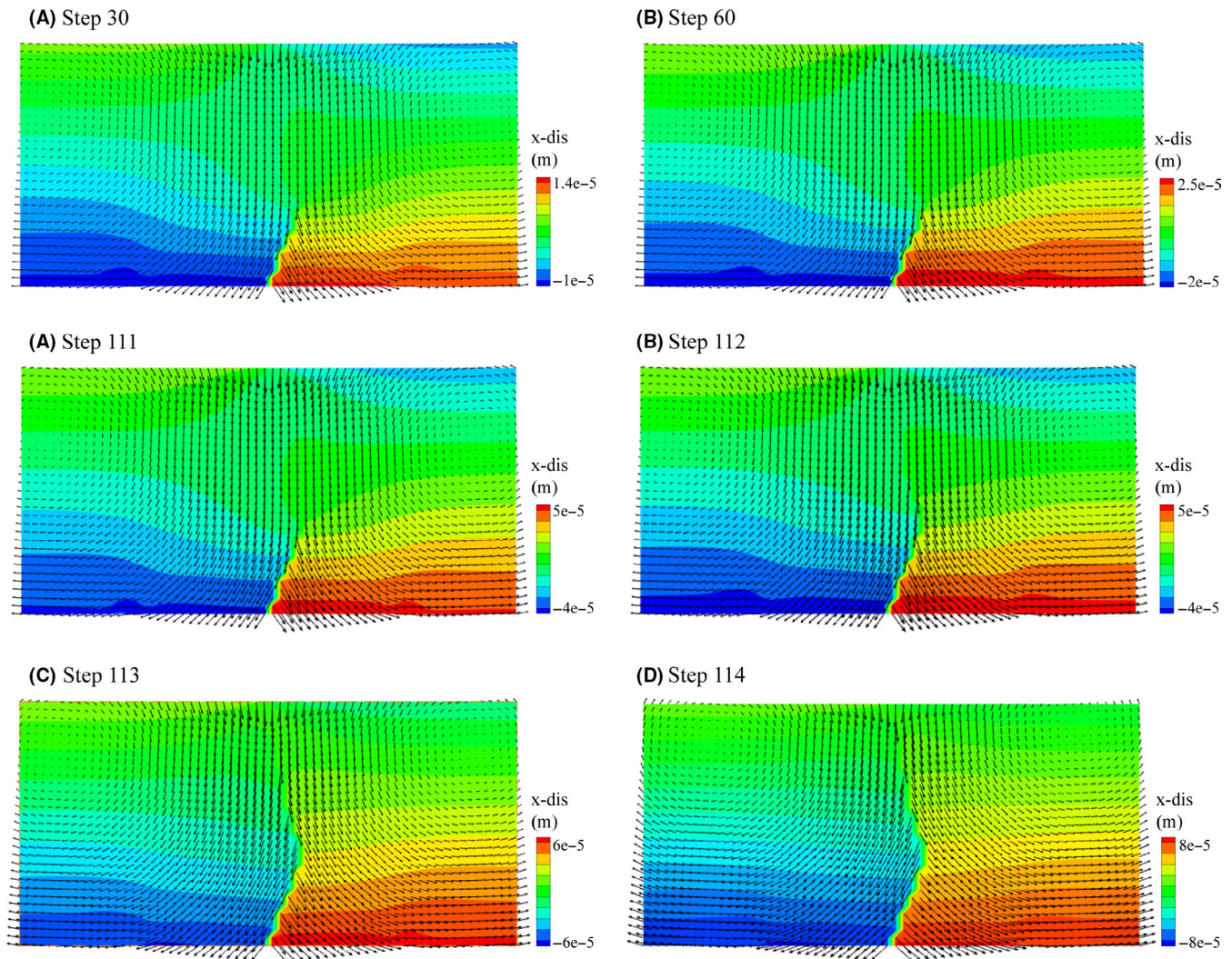
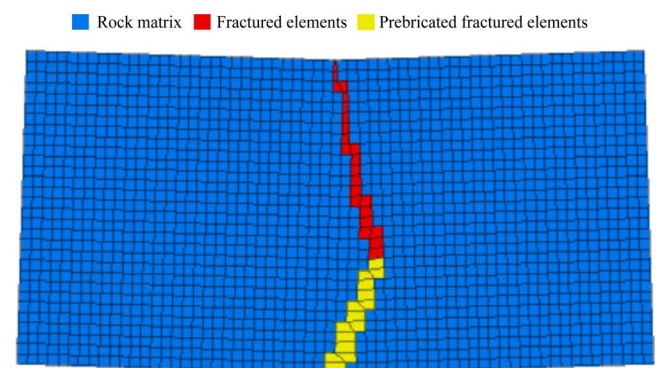


**FIGURE 9** The horizontal displacement distributions at different calculation steps ( $\alpha = 20^\circ$ )

specimen and platens are separated by the frictional interfaces with zero cohesion and the interface friction angle ( $\phi = 5^\circ$ , close to the real case). The elastic-plastic properties corresponding to the constitutive model are listed in Table 2. Note that all the presented models in this section below are run with the same parameters listed in Table 2. The only parameter that varies is dip angle  $\alpha$ , and its values are specified in the Figure 12. During the testing process, the downward velocity ( $V_z = -1 \times 10^{-6}$  m/s) is applied to the upper platen until the model fails.

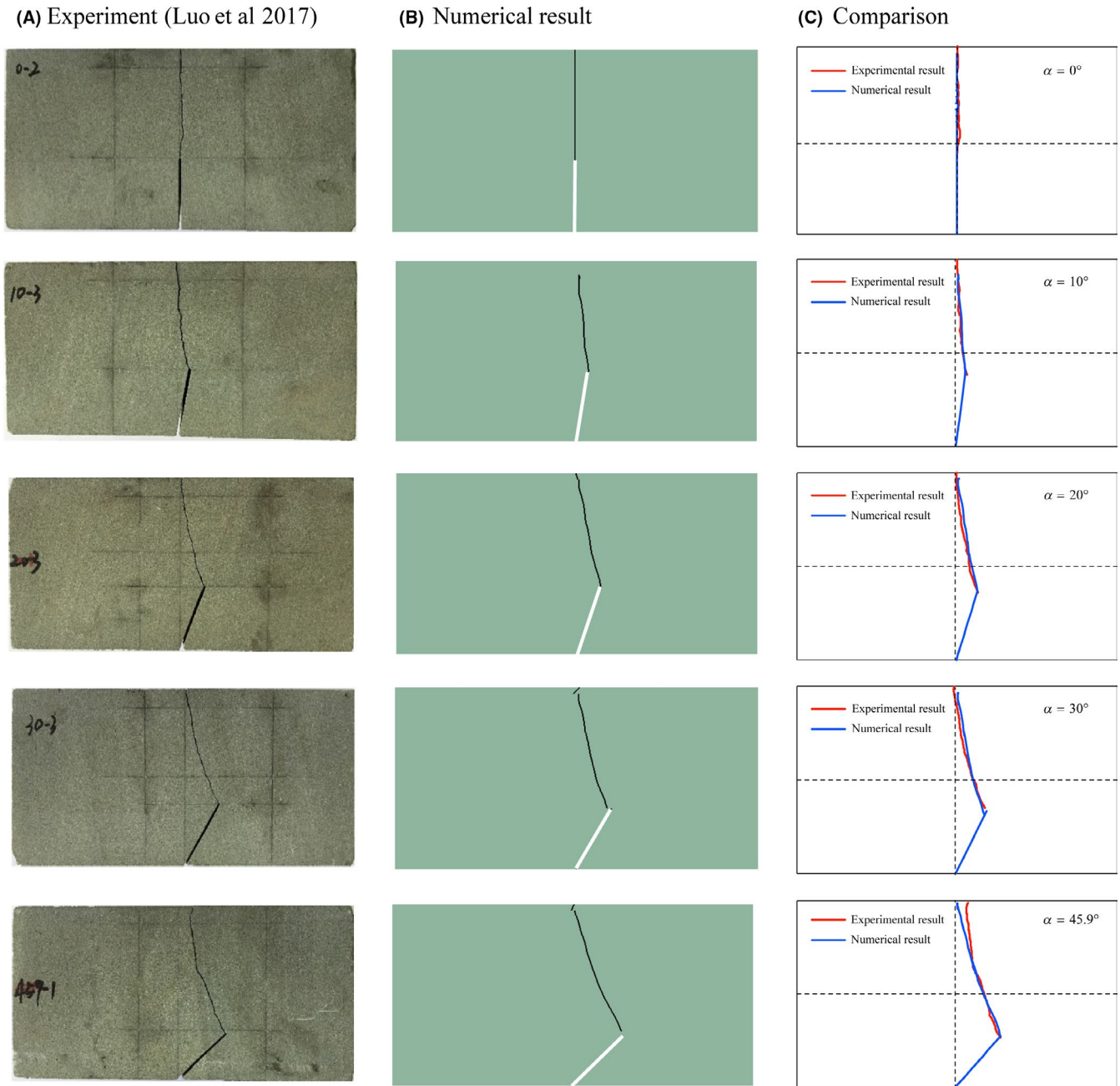
### 3.2.2 | Results

Figure 12A shows the numerical stress-strain curves of the specimens with one prefabricated flaw at different dip angles. It is apparent that the stress-strain curve first approximates a straight line corresponding to the linear elasticity and then exhibits a steep drop until the strain reaches a certain value, which captures well the postpeak characteristic



**FIGURE 10** The grid deformation (added by 10 times horizontal and vertical displacement) at  $\alpha = 20^\circ$

of the experimental result. Figure 12B shows that the peak stresses for experimental and numerical results are matched rather satisfactorily as well as its variation as the dip angle increases. For instance, the peak stress is minimum when the dip angle is  $60^\circ$ , which is also true for the numerical result.



**FIGURE 11** The failure outline: (A) experimental tests; (B) numerical simulation; (C) comparison

Figure 13 compares the horizontal displacement distribution for experimental and numerical results. It is shown that some discrepancies in displacement fields between experimental and numerical results exist clearly, but many experimental features are also numerically captured. For instance, the positions where the maximum displacements occur are similar. Overall, the numerical results capture well the real characteristics of experimental results.

As for fracture process, it can be observed from Figure 14 that on the whole, the fracture model could simulate the fracture process in the shear mode and even mixed mode (shear and tensile) well in comparison with experimental tests. However, there are still larger errors

in the fracture propagation path (than those in three-point bending tests) between experimental and numerical results. These errors might be due to heterogeneities of the specimen and pre-existing micro-fractures, which result in deviations at random for some degree along the propagation path. But in most cases, like experimental tests, the fractures numerically initiate from the vicinity of the pre-fabricated fracture tips and propagate along the loading direction to the upper and lower boundaries of the specimen. The evolution of the horizontal displacement distributions for different calculation steps at  $\alpha=30^\circ$  is presented in Figure 15. Overall, the numerical results in Figure 14A are reasonable.

**TABLE 2** Parameters for sandstone in uniaxial compression tests

Properties	$E$ , GPa	$\nu$	$c$ , MPa	$\alpha$ , °	$Ten$ , MPa	$\epsilon_{s,max}$	$\epsilon_{t,max}$
Specimen	28.7	0.23	16.59	20	2.5	$3.5 \times 10^{-3}$	$7.5 \times 10^{-3}$
Platen	200	0.1	-	-	-	-	-

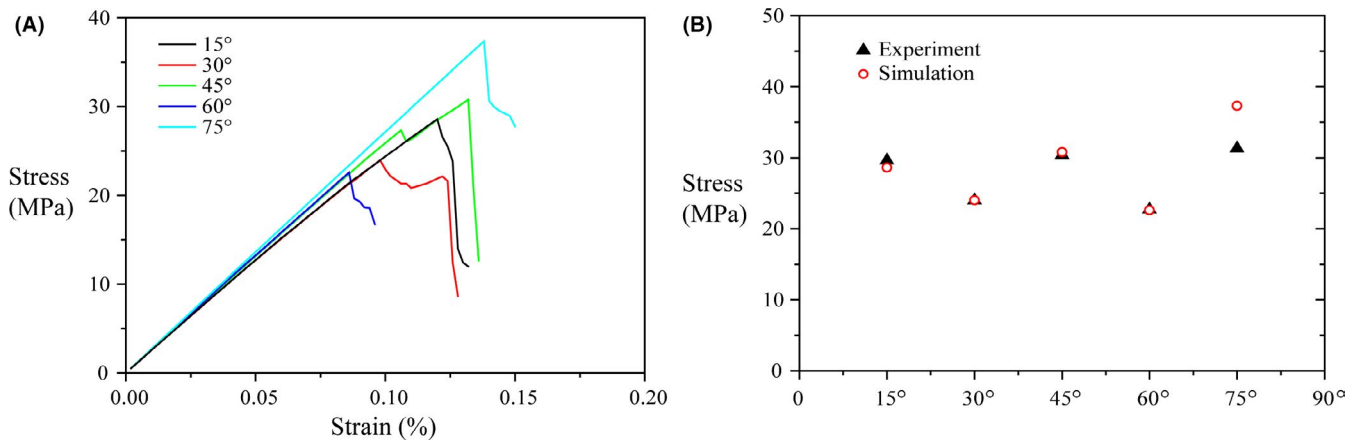
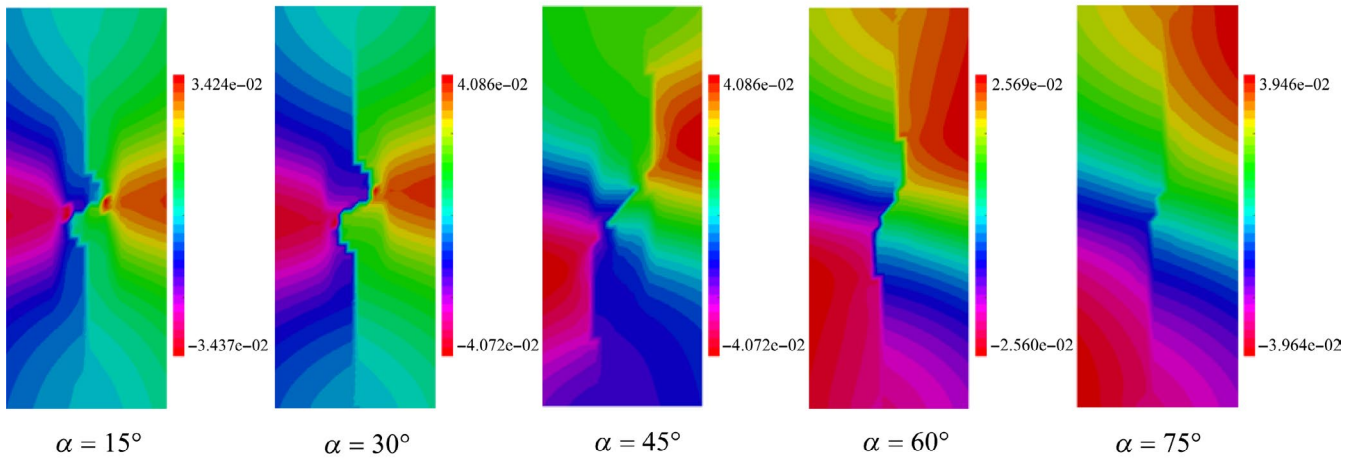


**FIGURE 12** The results of uniaxial compression tests at different dip angles: (A) stress-strain curves; (B) comparison of peak stresses between numerical and experimental tests

**(A) Numerical results - X Displacement (mm)**



**(B) Experiment (Zhao et al 2019)**

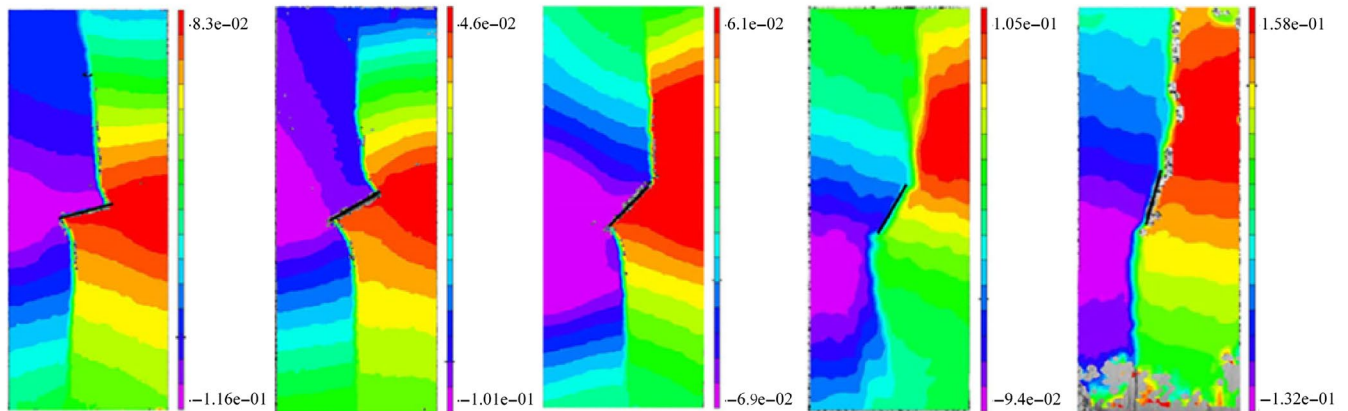


**FIGURE 13** The horizontal displacement distribution: (A) numerical simulation; (B) experimental tests

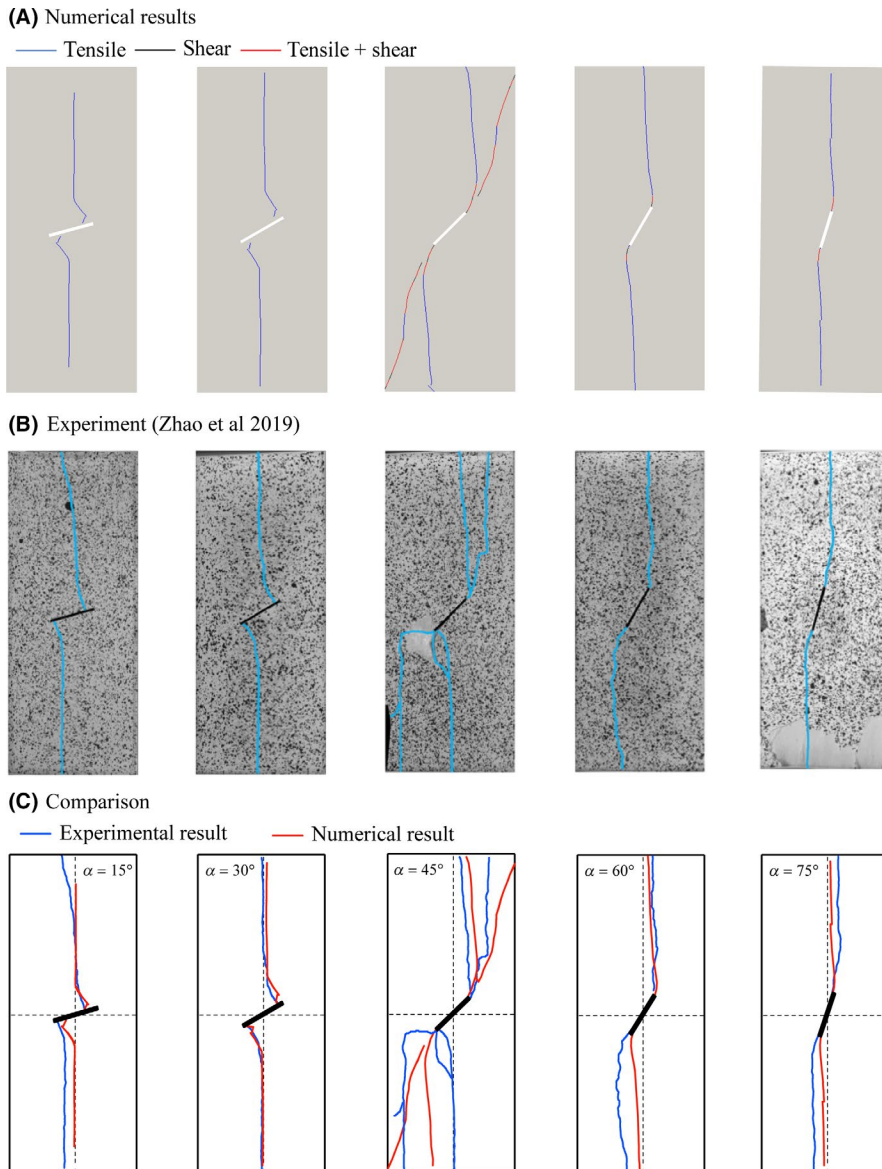


**FIGURE 14** The failure outline: (A) numerical simulation; (B) experimental tests; (C) comparison (tensile or shear means only tensile or shear failure occurs while tensile + shear means both tensile and shear occur in the fracture path)

Besides, the fracture propagation path was clearly marked into two modes to study the failure mode (tensile and shear modes, Figure 14A). The numerical results show that when the dip angles are small ( $15^\circ$  and  $30^\circ$ ), the failure modes are mainly tensile; when the dip angles are beyond  $30^\circ$ , the macroscopic fractures exhibit a mixture of tensile and shear characteristics and tensile fractures dominate over shear fractures. It indicates that failure mode does not remain constant but varies as dip angle increases.

In general, numerical results provide good fittings to not only three-point bending tests (specimen with one single flaw) but also uniaxial compression tests (specimen with one single flaw). This implies that the new fracture models proposed in this study are able to describe well the real characteristics related to the fracture initiation, propagation and the failure pattern in tensile mode, shear mode, and the mixed mode (tensile and shear).

## 4 | APPLICATION TO THE 2D PHYSICAL MODEL OF LONG-WALL MINING

### 4.1 | Modeling setup

A numerical model measuring  $5\text{ m} \times 0.4\text{ m} \times 1.85\text{ m}$  in  $x, y, z$  directions, respectively, is created in Flac3D to simulate the physical model performed by Kang et al.<sup>41</sup> The model contains mainly five rock seams: coal seam, fine sandstone, sandy mudstone, mudstone, siltstone, as shown in Figure 16. In the numerical model, the coal seam is at a depth of approximately  $0.275\text{ m}$  and has a thickness of  $0.15\text{ m}$ . Bedding planes are introduced as the ultrathin thin interlayer with elastic properties between different rock seams. The corresponding constitutive properties are listed in Table 3.

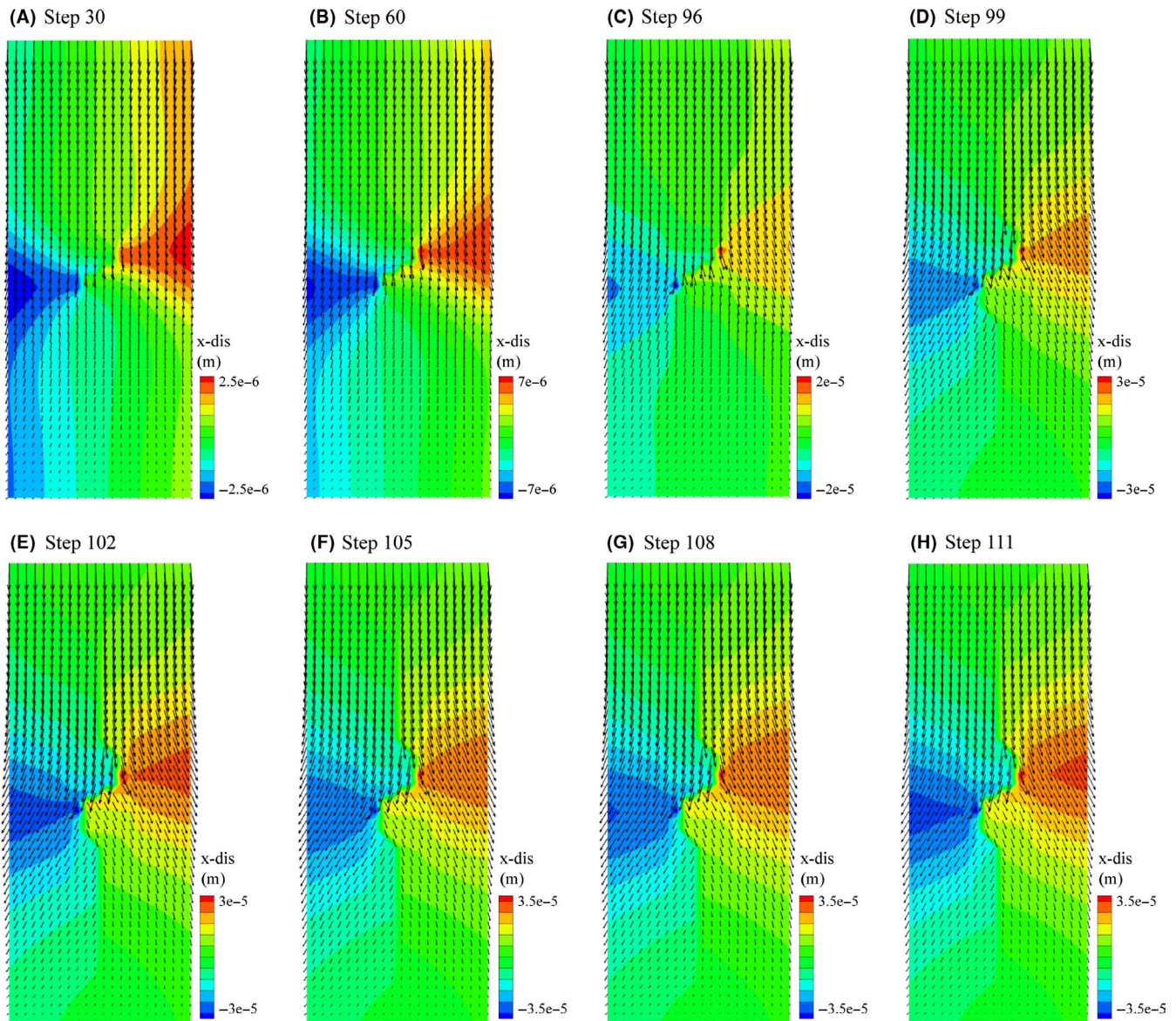
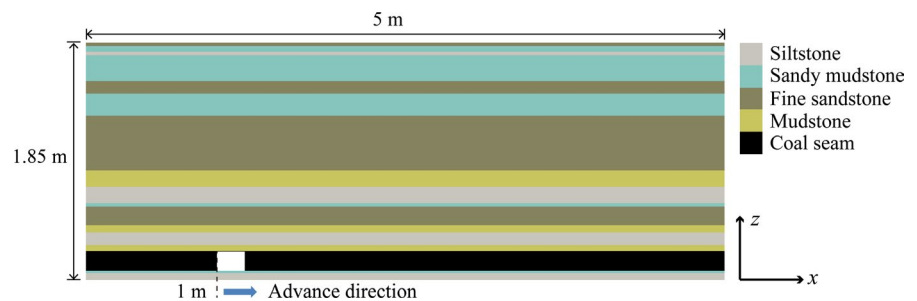


**FIGURE 15** The horizontal displacement distributions at different calculation steps ( $\alpha = 30^\circ$ )

**FIGURE 16** Modeling setup of long-wall mining



In this case, according to the boundary condition of the physical model, the vertical stress (0.23 MPa, in  $z$ -direction) is applied on the top of the model and the horizontal (in  $x$ -direction) stress imposed to the model was 0.27 MPa. The bottom of the model is fixed in its normal direction. The same stepwise caving process in the coal seam is simulated from the origin (the left side, 1 m) to the right side (4.1 m). Each step involves a 0.05 m advance and a total of 59 steps are imposed, which are the same as the physical

model. At each stage, sufficient calculation steps (17 000) have been performed to relieve stress and to allow the roof to cave.

## 4.2 | Results

Figure 17 provides illustrations of the numerical progressive roof failure. To gain more detailed information on fracture

Properties	$E$ , GPa	$\nu$	$c$ , MPa	$\alpha$ , °	$Ten$ , MPa	$\epsilon_{s,max}$	$\epsilon_{t,max}$
Coal	0.118	0.122	0.226	22.6	0.0639	8e-3	1e-4
Sandy mudstone	0.2	0.269	0.249	22.6	0.0748	8e-3	1e-4
Fine sandstone	0.371	0.089	0.358	22.6	0.0964	8e-3	1e-4
Siltstone	0.274	0.167	0.302	22.6	0.152	8e-3	1e-4
Mud	0.148	0.139	0.249	22.6	0.0497	8e-3	1e-4
Bedding plane	0.25	0.125	0.15	30	0		

**TABLE 3** Parameters for rocks in 2D long-wall mining

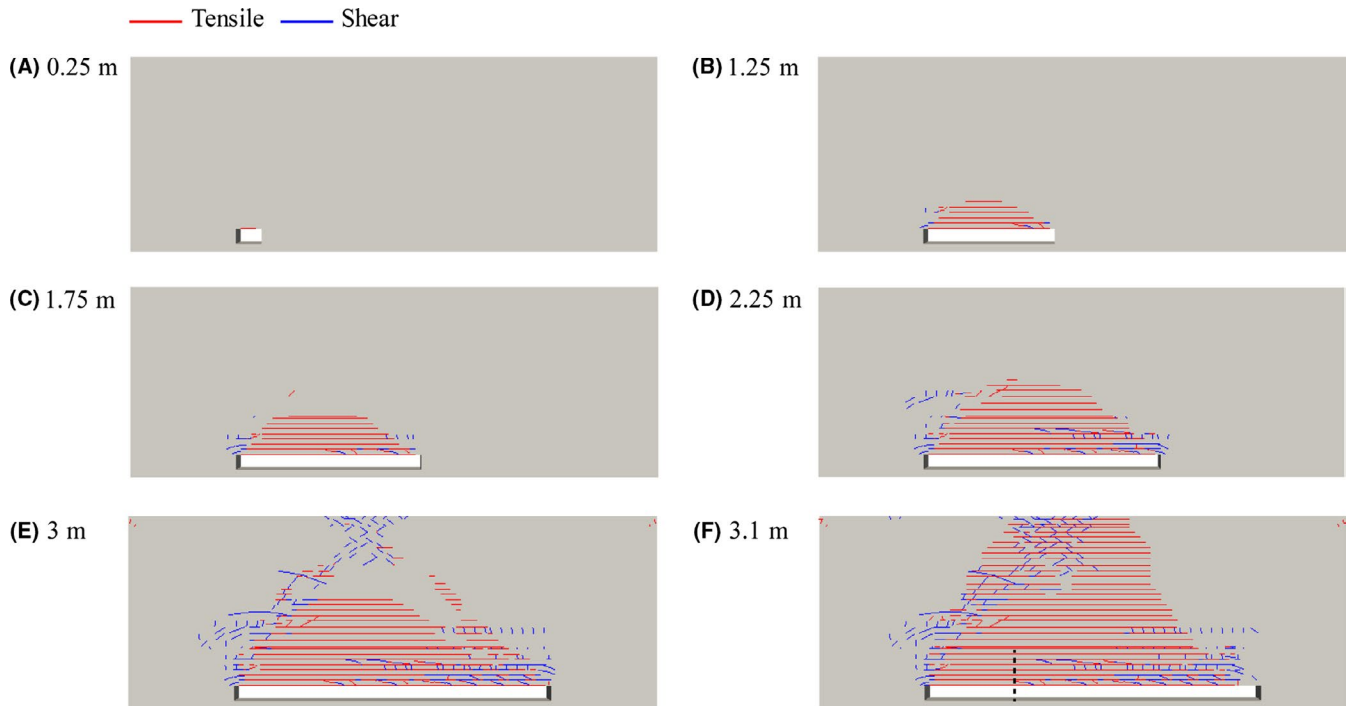


**FIGURE 17** Progressive roof failure at different stages

process, shear and tensile fractures are tracked during the calculation. Note that only the zones above coal seam are monitored. Blue lines stand for shear fractures while red lines represent tensile fractures. It can be found that, new shear fractures are generated in the overburden (in particular around the corner of roof) due to the stress concentration caused by the extraction process and then extend deeper into the roof as the face continues to advance. However, tensile fractures mainly appear in the form of bedding separation (the horizontal straight lines shown in Figure 17) because of the enhanced vertical subsidence (vertical displacement). This is so in the literature on long-wall mining researches.<sup>42</sup> Moreover, a comparison of the final fracture characteristics between the physical and numerical model is made in Figure 18. We can see that the numerically captured failure patterns and the experimentally captured failure patterns are rather similar on many aspects. Open fractures (characterized as the fractures in rock matrixes) zones located horizontally some distance above the immediate roof and vertically on the left side of the crushed roof, which is the similar case

for the physical model. The left and right dip angles of the crushed zones in numerical model are 61° and 57°, respectively, in comparison with 55° and 60° in the physical model. The larger discrepancy in left dip angle is attributed to the deviation in the center of subsidence area (Figure 19) and in the larger abutment pressure along the floor of coal seam near the left boundary of the model (Figure 20). Note that the abutment pressure distribution along the floor of coal seam (Figure 20) produced by simulation (dash line) approximates physical model (solid line) rather satisfactorily.

In addition, the initial fracture interval is numerically identified (dash line shown in Figure 17F). The main difference in failure pattern is that on the right side of this line the immediate roof shows crushed failure characteristics while bedding separation is the main failure type on the left side of this line. However, in physical modeling, the crushed failure is also observed on the left side of this line. The reason might be that in reality the roof strata on the left side of this line falls down and then broke into pieces due to the gravity effect, which is not captured in the simulation.

**FIGURE 18** The comparison of morphology characteristics at final stage: (A) local region of physical model; (B) physical model; (C) numerical simulation

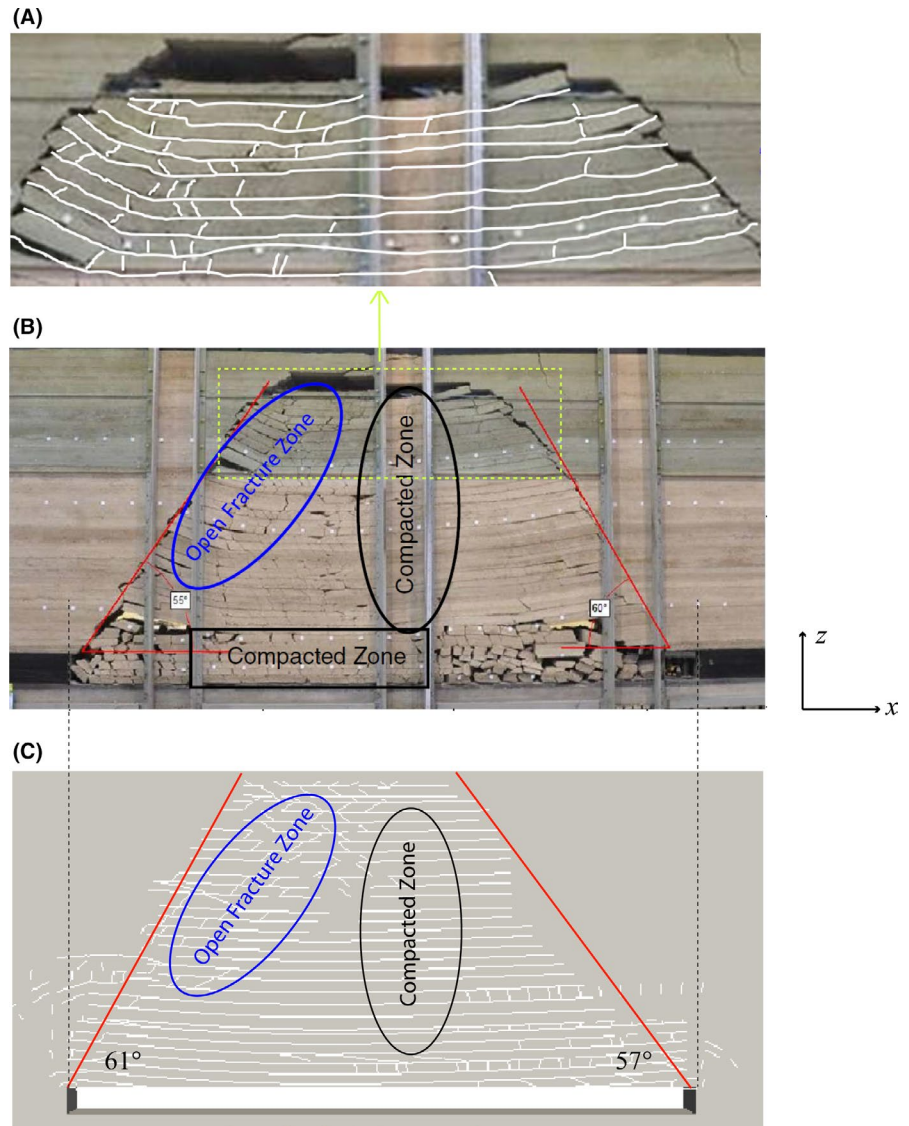
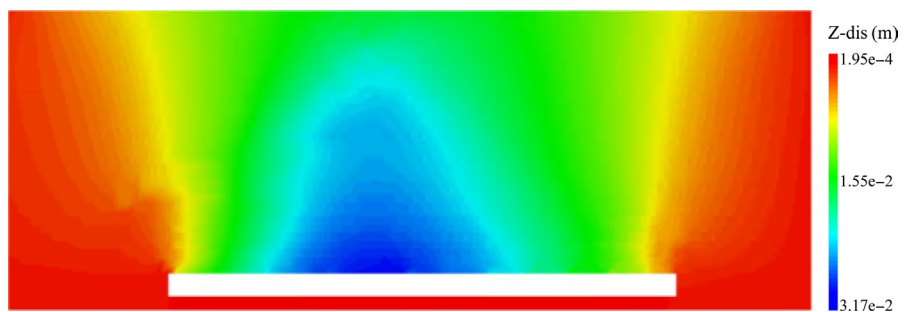


**FIGURE 19** Vertical displacement distribution at final stage



After statistics for rock matrixes, shear fractures dominate over tensile fractures by a ratio of approximately 10:1, which is in good agreement with numerical results (9:1, Gao et al<sup>42</sup>) and field observation.<sup>43</sup> Furthermore, herein, we define damage as the ratio of the number of fractured zones to that of total zones above the coal seam. Figure 21 displays the progressive damage during the mining process. All the three series of points (shear, tensile, and total) show the same trend but different slopes. The

function  $D_p(d)$  ( $D_p$  stands for progressive damage, and  $d$  is the mining distance) must meet the following requirements: (a) have qualitatively the same trend as the points in Figure 21; (b) the slope remains more or less constant at larger mining distance. The numerous trials have led to the following simple functions for shear Equation (17) and total damage Equation (18):

$$D_p^s = 26343.63d / (6.63 \times 10^6 - 1.65 \times 10^6 d) \quad (17)$$

$$D_p^{tot} = 9.94d / (1522.4 - 352.16d) \tag{18}$$

Note that  $d$  in the equations is limited due to the special experimental condition.  $D_p^s$  and  $D_p^{tot}$  represent shear and total damage, respectively. Shear damage shows a hyperbolic relationship with mining distance. And this is the case for total damage, which is reasonable on account that shear failure mode is dominant for rock matrix during the mining process. As for tensile damage, it is related to linear relationship:

$$D_p^t = 0.00291 + 0.00586d \tag{19}$$

where  $D_p^t$  is the tensile damage. Besides, the orientations of these fractures for rock matrices are also calculated in Figure 22.

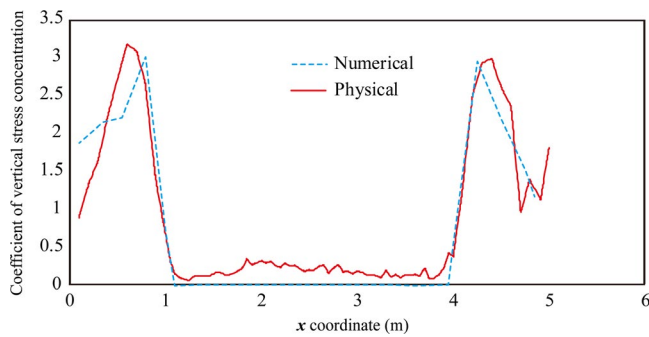


**FIGURE 20** Vertical stress distribution along the coal panel floor

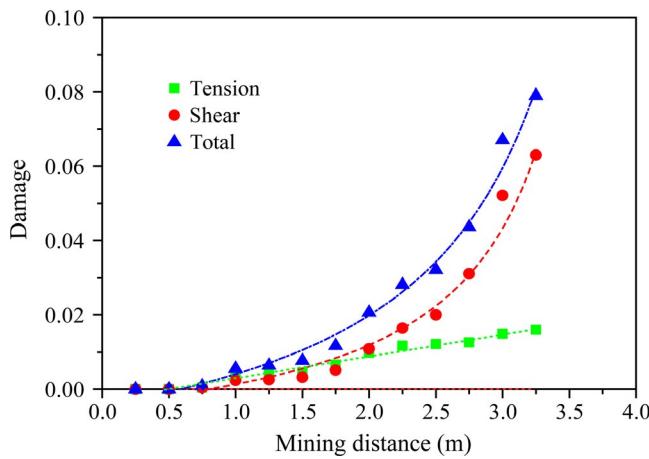


**FIGURE 21** Progressive damage during the mining

Most of the simulated fractures (shear and tensile) are oriented approximately 30° and 150° with respect to the horizontal line of roof, as can be observed in physical model (Figure 18A).

The modeling findings in this section show good accordance with the large-scale physical model. It indicates that the proposed constitutive models are able to reproduce the actual phenomenon for the 2D complex case in reality. The next section, therefore, moves on to discuss further 3D application of pillar failure, which is difficult to test via experiments.

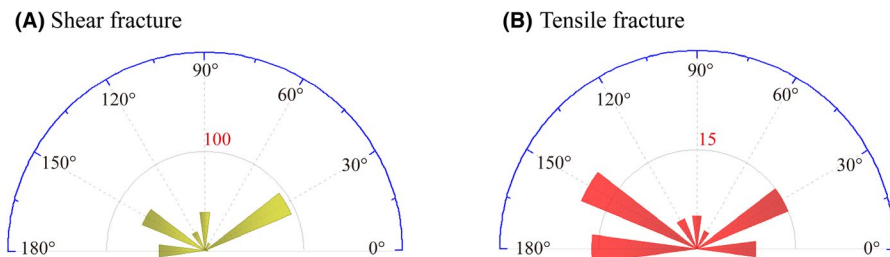
## 5 | APPLICATION TO 3D PILLAR FAILURE

### 5.1 | Modeling setup

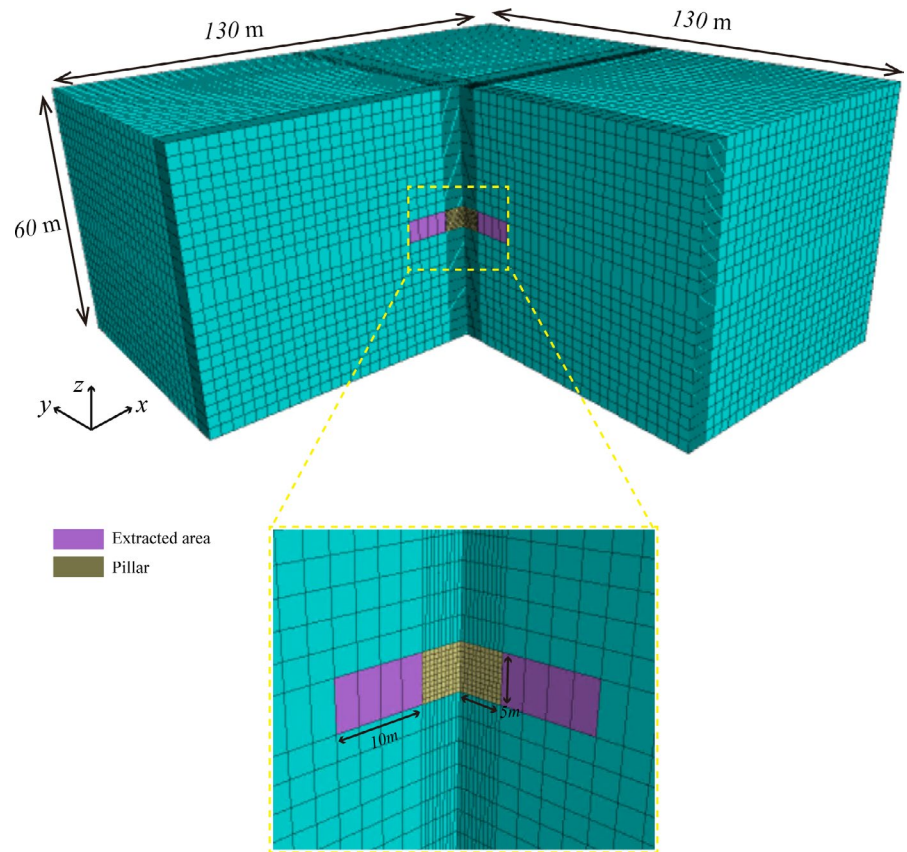
Generally, rock pillar has 3D geometries. Considering the effect of existing geological structure and in situ stress on the pillar behavior, a simply symmetric model (Figure 23) of a typical block caving pillar in an underground mine is analyzed. The mechanical properties are listed in Table 4. In this case, for boundary conditions, the displacements on each side of the model are fixed perpendicular to the direction of boundaries. The initial stresses imposed in the  $x$ -direction,  $y$ -direction and  $z$ -direction are 10 MPa, 10 MPa, and 15 MPa, respectively. The extracted area shown in Figure 23 will be first extracted, and then sufficient calculation steps (10 000) have been run for stress release and pillar failure.

### 5.2 | Results

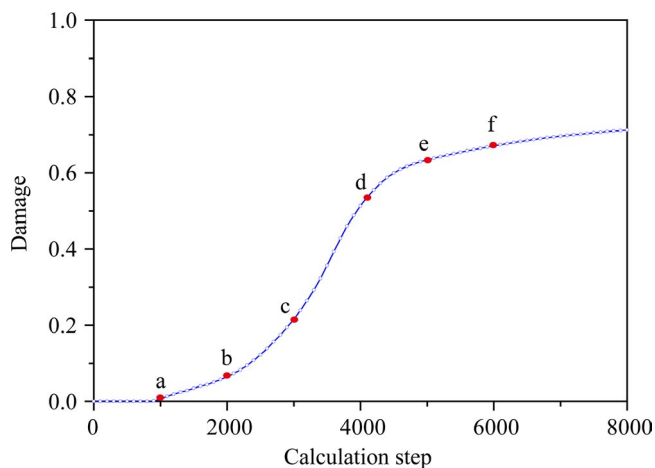
To quantitatively assess the degree of damage that pillar undergoes, the ratio of fractured zones to total zones in the pillar is computed and illustrated in Figure 24. The curve in Figure 24 depicts that firstly there is no damage after the extracted area is immediately extracted; then the slope increases due to the progressive generation of fractures; after reaching a certain damage, there is a rapid reduction in the slope; lastly, the slope remains more or less constant. The contours of the maximum principal stress corresponding six points marked in Figure 24 are drawn in Figure 25. It depicts that as calculation step continues, distressed region (corresponding to fractured region in Figure 26) appears at the corner of the



**FIGURE 22** Statistics of orientations of fractures for rock matrices: (A) shear fracture; (B) tensile fracture

**FIGURE 23** Modeling setup of the pillar**TABLE 4** Parameters for the rock in 3D pillar failure

Properties	$E$ , GPa	$\nu$	$c$ , MPa	$\alpha$ , °	$Ten$ , MPa	$\epsilon_{s,max}$	$\epsilon_{t,max}$
Specimen	9	0.25	3.26	33	0.9	4e-3	1e-3

**FIGURE 24** Progressive damage of pillar failure

pillar surface, then extend to the entire surface and eventually propagate toward the core. Figure 27 shows the progressive outlines of the fractures at different cross sections. We can see from Figure 27 that fractures firstly are generated at the corner of the pillar corresponding to the slabbing in situ and

similar results are also obtained by Wagner,<sup>44</sup> then fractures extend to the center of the pillar corresponding to continued spalling in situ; lastly the pillar forms a “hourglass” failure shape (Figure 26). These findings above are in well keeping with the numerical observations of Sainoki and Mitri<sup>45</sup> and the field observations of Pritchard and Hedley.<sup>46</sup> These results indicate the models proposed are capable of dealing with 3D engineering cases.

## 6 | CONCLUDING DISCUSSION

The impact of discontinuities such as fractures, joints and fault on mechanical behaviors has been long known from the experimental and numerical information. These results show discontinuities could strongly affect rock properties including strength, deformability and fracture process, etc. Traditionally, plastic damage are often employed to describe these effects of discontinuities in plastic constitutive models. Generally, this approach used in plastic models is capable of providing good explanations in many topics related to rock mechanics. However, since in reality the contact state of

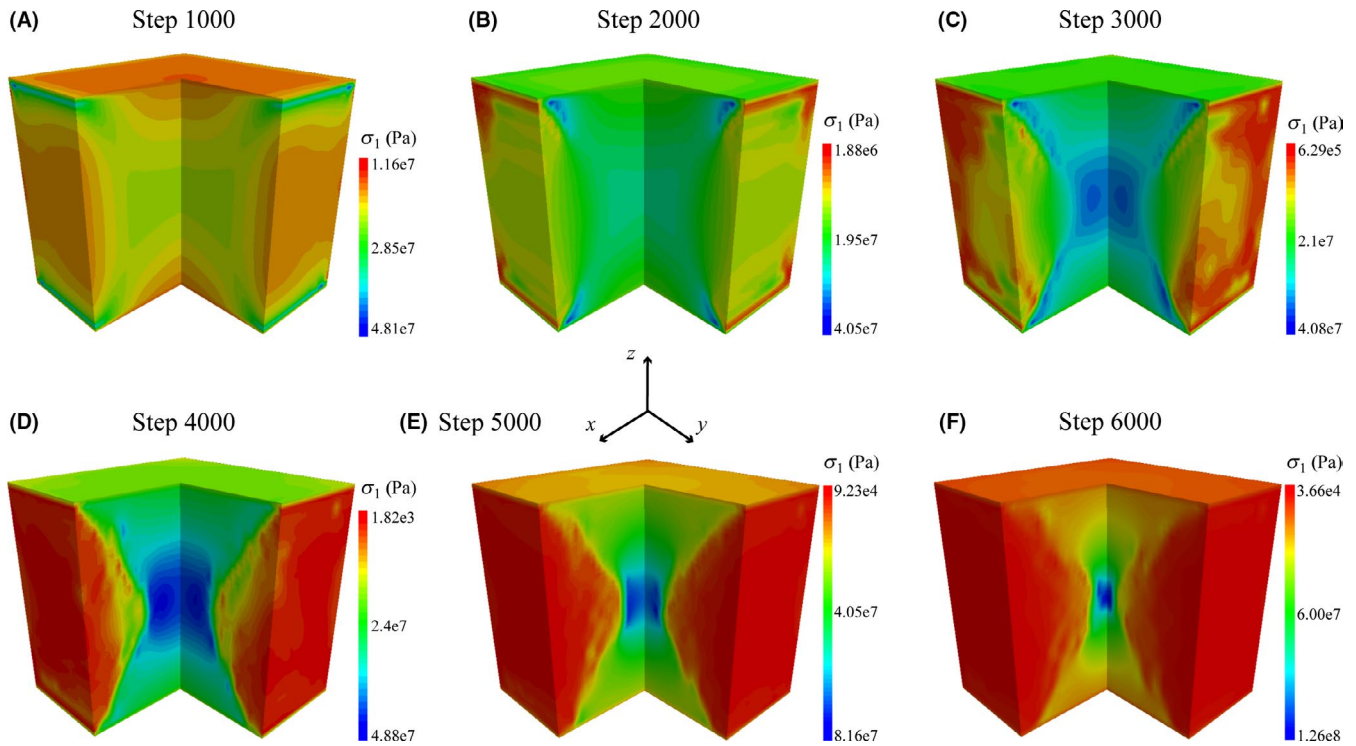


**FIGURE 25** The contour of the maximum compression stress at the points marked on damage curve in Figure 24

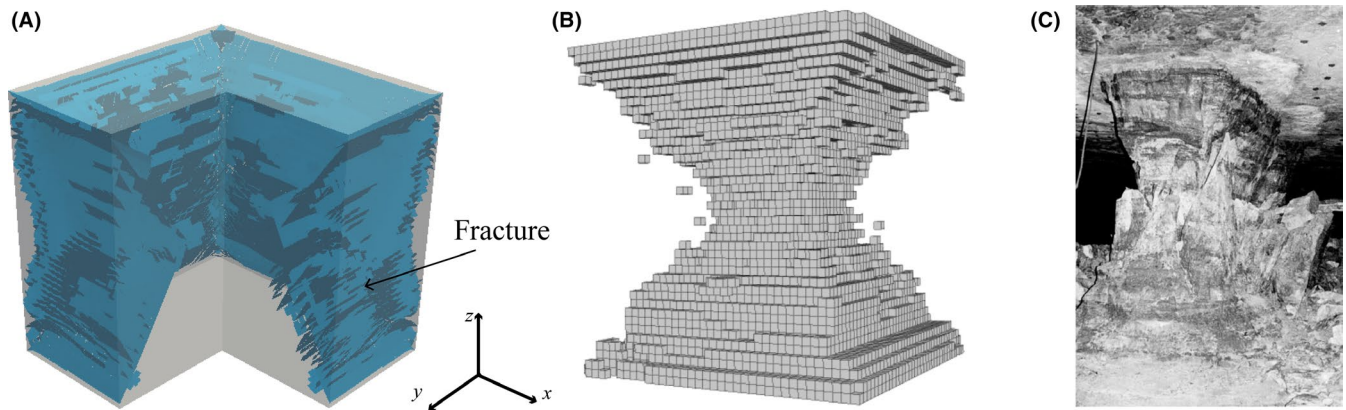
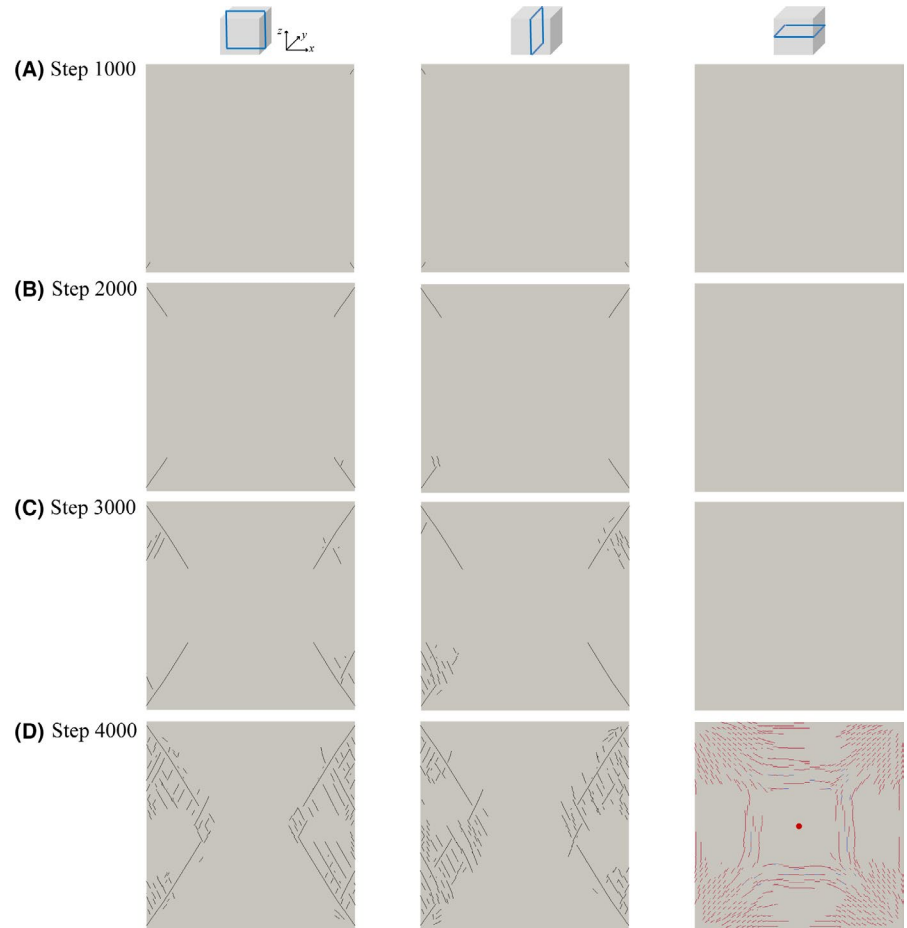


**FIGURE 26** 3D failure shape comparison at point d in Figure 24: (A) numerical fracture shape; (B) zones without fracture; (C) field observation<sup>46</sup>

fractures constantly changes from contact to noncontact state (or from noncontact to contact state), these plastic models are not completely reasonable. This study therefore proposes a quasi-continuum model by considering the mechanical behaviors of fractures for both contact and noncontact states. Using the finite-difference code Flac3D as the numerical tool, the present study efficiently simulates the influence of discontinuities on fracture process in a rock. Then, this model is adopted to a 2D complex long-wall mining case and a 3D simple case of a typical block caving pillar. The obtained simulation results are in general agreement with the physical model and field monitoring. The specific conclusions are as follows:

1. Fracture processes including fracture initiation and propagation in three-point bending and uniaxial compression tests have been successfully reproduced with the proposed fracture constitutive model. It indicates this model can be utilized to simulate fracture processes in the tensile, shear, and mixed modes.
2. During the long-wall mining, shear fractures dominate over tensile fractures (mainly generated in form of bedding separations) in terms of rock matrixes. The most majority of fractures are orientated at  $30^\circ$  and  $150^\circ$  with respect to the horizontal roof line. This might be particularly useful in explaining the permeability anisotropy and predicting methane migration in situ but not discussed in detail here.

**FIGURE 27** The progressive failure outlines for different cross sections at different stages corresponding to the points marked in Figure 24



3. The pillar experiences three stages (slow-growth damage; accelerated-growth damage; constant-growth damage) before failure. The obtained results of 3D case indicate the proposed model is capable of simulating the fracture initiation and propagation on 3D scale.

Overall, the proposed model could provide a new way to simulate the fracture initiation and propagation in many fields where fracture behaviors need be taken into account. Further work is required to clearly identify the limits of the proposed model and investigate some more complex engineering applications in particular in fully 3D scale.

#### ACKNOWLEDGMENTS

The work presented in this study is funded by the National Natural Science Foundation of China (no. 51774056; no. 51974042), the Chongqing Research Program of Basic Research and Frontier Technology (no. cstc2017jcyjB0252), the National Science Fund for Distinguished Young Scholars of China (No. 51625401) and the Chongqing University Postgraduates' Innovation Project (CYB17047).

#### CONFLICT OF INTEREST

The authors declare that they have no conflict of interest.

#### ORCID

Junchao Chen  <https://orcid.org/0000-0003-3737-3188>

Binwei Xia  <https://orcid.org/0000-0002-8928-0461>

Zhonghui Shen  <https://orcid.org/0000-0001-8009-9167>

#### REFERENCES

1. Dugdale DS. Yielding of steel sheets containing slits. *J Mech Phys Solids*. 1960;8:100-104.
2. Griffith AA. The phenomena of rupture and flow in solids. *Philos T R Soc*. 1921;221:163-198.
3. Horii H, Nematnasser S. Compression-induced microcrack growth in brittle solids: axial splitting and shear failure. *J Geophys Res*. 1985;90(NB4):3105-3125.
4. Irwin GR. Relation of stresses near a crack to the crack extension force. In: *9th International Congress of Applied Mechanics*. Brussels; 1957.
5. Park CH, Bobet A. Crack initiation, propagation and coalescence from frictional flaws in uniaxial compression. *Eng Fract Mech*. 2010;77:2727-2748.
6. Goncalves da Silva B, Einstein HH. Modeling of crack initiation, propagation and coalescence in rocks. *Int J Fract*. 2013;182:167-186.
7. Brace WF, Bombolakis EG. A note on brittle crack growth in compression. *J Geophys Res*. 1963;68:3709-3713.
8. Lajtai EZ. Brittle fracture in compression. *Int J Fracture*. 1974;10:525-536.

9. Wong LNY, Einstein HH. Crack coalescence in molded gypsum and carrara marble: part 2 microscopic observations and interpretation. *Rock Mech Rock Eng.* 2009;42:513-545.
10. Fan LF, Wu ZJ, Wan Z, Gao JW. Experimental investigation of thermal effects on dynamic behavior of granite. *Appl Therm Eng.* 2017;125:94-103.
11. Haeri H, Shahriar K, Marji MF, Moarefvand P. Experimental and numerical study of crack propagation and coalescence in pre-cracked rock-like disks. *Int J Rock Mech Min Sci.* 2014;67:20-28.
12. Tarokh A, Blanksma DJ, Fakhimi A, Labuz JF. Fracture initiation in cavity expansion of rock. *Int J Rock Mech Min Sci.* 2016;85:84-91.
13. Zhao C, Zhou YM, Zhao CF, Bao C. Cracking processes and coalescence modes in rock-like specimens with two parallel pre-existing cracks. *Rock Mech Rock Eng.* 2018;51:3377-3393.
14. Zhao C, Niu JL, Zhang QZ, Zhao CF, Zhou YM. Failure characteristics of rock-like materials with single flaws under uniaxial compression. *B Eng Geol Environ.* 2019;78:593-603.
15. Lin Q, Labuz JF. Fracture of sandstone characterized by digital image correlation. *Int J Rock Mech Min Sci.* 2013;60:235-245.
16. Shen BT, Stephansson O, Einstein HH, Ghahreman B. Coalescence of fractures under shear stresses in experiments. *J Geophys Res.* 1995;100:5975-5990.
17. Hou ZM, Zhou L, Kracke T. Modelling of seismic events induced by reservoir stimulation in an enhanced geothermal system and a suggestion to reduce the deformation energy release. In: *Proceedings of 1st International Conference on Rock Dynamics and Applications. Switzerland*; 2013.
18. Li LC, Tang CA, Tham LG, Yang TH, Wang SH. Simulation of multiple hydraulic fracturing in non-uniform pore pressure field. *Adv Mater Res.* 2005;9:163-172.
19. Rutqvist J, Wu YS, Tsang CF, Bodvarsson G. A modeling approach for analysis of coupled multiphase fluid flow, heat transfer, and deformation in fractured porous rock. *Int J Rock Mech Min Sci.* 2002;39:429-442.
20. Tang C, Tham L, Lee P, Yang T, Li L. Coupled analysis of flow, stress and damage (FSD) in rock failure. *Int J Rock Mech Min Sci.* 2002;39:477-489.
21. Bandis SC, Lumsden AC, Barton NR. Fundamentals of rock joint deformation. *Int J Rock Mech Min Sci Geomech Abstr.* 1983;20:249-268.
22. Li SB, Li X, Zhang DX. A fully coupled thermo-hydro-mechanical, three-dimensional model for hydraulic stimulation treatments. *J Nat Gas Sci Eng.* 2016;34:64-84.
23. Nassir M, Settar A. Prediction of stimulated reservoir volume and optimization of fracturing in tight gas and shale with a fully elasto-plastic coupled geomechanical model. In: *Proceeding of the SPE Hydraulic Fracturing Technology. Woodlands, USA*; 2013.
24. Gui YL, Zhao ZY, Zhang C, Ma SQ. Numerical investigation of the opening effect on the mechanical behaviours in rocks under uniaxial loading using hybrid continuum-discrete element method. *Comput Geotech.* 2017;90:55-72.
25. Lee C, Cundall PA, Potyondy DO. Modeling rock using bonded assemblies of circular particles. In: *North American Rock Mechanics Symposium. Montreal*; 1996.
26. Li HQ, Wong LNY. Numerical study on coalescence of pre-existing flaw pairs in rock-like material. *Rock Mech Rock Eng.* 2014;47:2087-2105.
27. Tang CA, Lin P, Wong RHC, Chau KT. Analysis of crack coalescence in rock-like materials containing three flaws-part 2: numerical approach. *Int J Rock Mech Min Sci.* 2001;38:925-939.
28. Yang L, Jiang YJ, Li SC, Li B. Experimental and numerical research on 3D crack growth in rocklike material subjected to uniaxial tension. *J Geotech Geoenviron.* 2013;139:1781-1788.
29. Yang W, Luo G, Duan K, et al. Development of a damage rheological model and its application in the analysis of mechanical properties of jointed rock masses. *Energy Sci Eng.* 2019;7:1016-1031.
30. Zhao C, Matsuda H, Morita C, Shen MR. Study on failure characteristic of rock-like materials with an open-hole under uniaxial compression. *Strain.* 2011;47:405-413.
31. Zhang XP, Zhang Q, Wu SC. Acoustic emission characteristics of the rock-like material containing a single flaw under different compressive loading rates. *Comput Geotech.* 2017;83:83-97.
32. Belytschko T, Black T. Elastic crack growth in finite elements with minimal remeshing. *Int J Numer Meth Eng.* 1999;45:601-620.
33. Moes N, Dolbow J, Belytschko T. A finite element method for crack growth without remeshing. *Int J Numer Meth Eng.* 1999;46:131-150.
34. Wagner GJ, Moes N, Liu WK, Belytschko T. The extended finite element method for rigid particles in Stokes flow. *Int J Numer Meth Eng.* 2001;51:293-313.
35. Watanabe N, Wang W, Taron J, Gorke UJ, Kolditz O. Lower dimensional interface elements with local enrichment: application to coupled hydro-mechanical problems in discretely fractured porous media. *Int J Numer Methods Eng.* 2012;90:1010-1034.
36. Itasca Consulting Group. *FLAC 3D (Fast Lagrangian Analysis of Continua in 3-dimensions) 5.0 Manual*; 2013.
37. Zhou L, Su XP, Hou ZM, Lu YY, Gao Y. Numerical investigation of the hydromechanical response of a natural fracture during fluid injection using an efficient sequential coupling model. *Environ Earth Sci.* 2016;75:1263.
38. Zhou L, Su XP, Lu YY, Ge ZL, Zhang ZY, Shen ZH. A new three-dimensional numerical model based on the equivalent continuum method to simulate hydraulic fracture propagation in an underground coal mine. *Rock Mech Rock Eng.* 2019;52:2871-2887.
39. Goodman RE. A model for the mechanics of jointed rock. *J Soil Mech Found.* 1968;94:637-660.
40. Luo Y, Ren L, Xie LZ, Ai T, He B. Fracture behavior investigation of a typical sandstone under mixed-mode loading using the notched deep beam bending method. *Rock Mech Rock Eng.* 2017;50:1987-2005.
41. Kang HP, Lou JF, Gao FQ, Yang JH, Li JZ. A physical and numerical investigation of sudden massive roof collapse during longwall coal retreat mining. *Int J Coal Geol.* 2018;188:25-26.
42. Gao FQ, Doug S, Kang HP. Simulation of roof shear failure in coal mine roadways using an innovative UDEC Trigon approach. *Comput Geotech.* 2014;61:33-41.
43. Kelly M, Luo X, Craig S. Integrating tools for longwall geomechanics assessment. *Int J Rock Mech Min Sci.* 2002;39:661-676.
44. Wagner H. Determination of the complete load-deformation characteristics of coal pillars. In: *Proceedings of 3rd ISRM Conference. Denver, Colorado*; 1974.

45. Sainoki A, Mitri HS. Numerical investigation into pillar failure induced by time-dependent skin degradation. *Int J Min Sci Tech.* 2017;27:591-597.
46. Pritchard CJ, Hedley DGF. Progressive pillar failure and rock bursting at Denison Mine. In: *Proceedings of the 3rd International Symposium on Rock Bursts and Seismicity in Mines.* Kingston; 1993.

**How to cite this article:** Chen J, Zhou L, Chemenda AI, Xia B, Su X, Shen Z. Numerical modeling of fracture process using a new fracture constitutive model with applications to 2D and 3D engineering cases. *Energy Sci Eng.* 2020;8:2628–2647. <https://doi.org/10.1002/ese3.690>